PAPER

Check for updates

Synthesis of MoS$_2$/MoO$_3$ nano-heterojunction towards enhanced photocatalytic activity under LED light irradiation *via in situ* oxidation sintering†

Jianfeng Qiu, [ID] [ab] Yanping Liu, [b] Minxian Cao, [b] Luqi Xie, [b] Yongkun Liu, [b] Hongwen Li, [b] Junqiang Lu, [b] Qifeng Liang, [b] Jiaqi Pan [ID] [ac] and Chaorong Li[*a]

The MoS$_2$/MoO$_3$ nano-heterojunction photocatalyst was synthesized *via* the *in situ* oxidation sintering method. The properties of the samples were characterized by XRD, SEM, EDX, TEM, UV-vis, PL, FT-IR, BET and electrochemical techniques. The MoS$_2$/MoO$_3$ nano-heterojunction (MS-400) exhibited significantly better photocatalytic activity toward Rhodamine B degradation (0.42634 h^{-1}) than monomer MoS$_2$ (~8.0-folds) and MoO$_3$ (~25.6-folds). This is mainly attributed to the MoS$_2$/MoO$_3$ heterojunction interface having an appropriate potential gradient that can promote the interface carrier transportation/separation to optimize the carrier efficiency and increase the solar absorption and specific surface areas/active sites *via* microstructures.

1. Introduction

With the increasing concern over environmental degradation, the use of semiconductor photocatalysts to degrade organic pollutants in water has been rapidly developed in recent years.[1–5] It has been shown that heterogeneous photocatalytic oxidation based on oxides is one of the most promising methods for the treatment of water pollutants due to its suitable potential structure for pollutant oxidation and its excellent stability for long-term applications.[6–10] However, solar energy is inefficient because of the wider bandgap and the high carrier recombination, limiting its further commercialization. Therefore, the light absorption and carrier efficiency must be developed so that the drawbacks of most oxides can be overcome.[11,12] So far, semiconductor photocatalysts, such as Ag-based,[13–15] Bi$_2$WO$_6$-based[16,17] and g-C$_3$N$_4$-based photocatalysts,[18,19] have been reported to exhibit remarkable visible photocatalytic activity.

Notably, molybdenum (Mo) oxides and sulfides have attracted growing research interest as promising electrocatalysts and photocatalysts owing to their unique electronic structures and surface active sites. They are even being explored as photo-electrocatalysts for a variety of applications in addressing environmental and energy issues.[20–22] Molybdenum sulfide (MoS$_2$) is a well-studied semiconductor with superior catalytic properties and stability and is extensively used as active materials in photo-electrocatalysis, sensors, supercapacitors and lithium ion batteries. In particular, the few-layered 2H-MoS$_2$, as a n-type semiconductor, possesses unique optical properties such as a layer-modulated narrow band gap,[23] strong light–matter interaction,[24] and anti-photocorrosion[25,26] and has been illustrated to be a better catalyst for visible-light-driven photocatalysis, *e.g.*, CuS/MoS$_2$,[27] Au/MoS$_2$,[28] Ag/MoS$_2$ (ref. 29) and MoS$_2$/graphene.[30] In addition, the few-layered MoS$_2$ with sufficient surface areas and edges can provide numerous active sites. It can also promote carrier diffusion and decrease the overpotential for accelerating the photocatalytic process.[31] However, as a monomer photocatalyst, the high carrier recombination and low carrier mobility have restricted its further applications. Thus, further improvement would be necessary, such as surface modification, doping, or barrier regulation. As reported previously, for a heterojunction, the electric field force caused by an intrinsic built-in electric field can rapidly drive the transfer and separation of electrons and holes, forming a region of space charge that enhances the carrier concentration and mobility for effectively improving the carrier. This development opens up new avenues for solar-driven photocatalytic water splitting and wastewater treatment, offering sustainable solutions for generating clean energy and addressing water pollution challenges.

Matched heterojunction materials are clearly important. Molybdenum trioxide (MoO$_3$), as an intrinsic n-type semiconductor, possesses a suitable band gap of approximately 2.89 eV, matched crystalline structure and homologous Mo-based compound.[32] MoO$_3$ is deemed as one of the most matched layered transition-metal oxides to form a surface

[a] College of Textile Science and Engineering, Zhejiang Sci-Tech University, Hangzhou, 310018, P. R. China. E-mail: crli@zstu.edu.cn

[b] Department of Physics, Shaoxing University, Shaoxing, 312000, P. R. China

[c] Key Laboratory of Optical Field Manipulation of Zhejiang Province, Department of Physics, Zhejiang Sci-Tech University, Hangzhou, 310018, P. R. China

heterojunction, showing high stability and high-quality,[33] including for use as an interconnection layer for polymer tandem solar cells or pseudocapacitors.[34,35] Moreover, the surface MoO_3-based heterojunction modification with remarkable light absorption can further enhance the solar efficiency, as well as provide a mass of activated carrier injection caused by Mo^{6+} ions for improving the carrier efficiency.[36,37] Furthermore, the good physical–chemical stability can effectively enhance the photocatalytic stability for actual applications.[38–40]

In this work, we discover the novel photocatalyst MoS_2/MoO_3 type II heterojunction[41,42] using the simple *in situ* oxidation sintering method. Significantly, molybdenum oxide and molybdenum sulfide share the same Mo-based cation, providing a more intimate heterojunction interface in the formed type II heterojunction for accelerating the carrier separation and inhibiting recombination. Furthermore, a series of characteristics were detected by SEM, HRTEM, XPS, among other methods. The results clearly showed that the obtained MoS_2/MoO_3 heterojunction (MS-400) had excellent photocatalytic activity toward Rhodamine B degradation under LED light irradiation.

2. Experimental

All of the reagents were used directly without further purification after purchase. Molybdenum disulfide (MoS_2, 99.5%) was purchased from Shanghai Aladdin Biochemical Technology Co., Ltd (Shanghai, China). A weighed mass of 0.5 g MoS_2 was added to the bottom of an alundum crucible. It was then placed into a muffle furnace, heated at a rate of 5 °C min^{-1} in air, and kept at a certain temperature for 1 h. Subsequently, the sample was cooled to room temperature naturally, and the holding temperature was changed. The samples obtained at different sintering temperatures were respectively named MS-300, MS-350, MS-400, MS-450, MS-500 and MS-600, and the original molybdenum disulfide was labelled as MS-0.

Further details and characterizations are shown in ESI.†

3. Results and discussion

3.1 Structure of the photocatalyst

The XRD pattern is shown in Fig. 1. The diffraction patterns for MS-0 and MS-300 exhibit sharp and intense peaks at 14.38°,

32.68°, 39.54°, 44.15° and 49.79°, corresponding to the (002), (100), (103), (006) and (105) planes of MoS_2 (JPCDS 37-1492), respectively. This indicates that the *in situ* oxidation process does not occur before 300 °C. With the increase of sintering temperature, the new diffraction peaks at 12.72°, 23.28°, 25.69° and 27.28° clearly correspond to MoO_3 (JPCDS 76-1003), indicating the proceeding of the *in situ* oxidation process. Correspondingly, the peaks of MoS_2 gradually diminish. These results correspond with the Raman and FTIR spectral information shown in Fig. S1 and S2,† respectively. The grain size of the sample by Scherrer formula is also consistent with it (Fig. S3†). It is worth noting that the mass also begins to decrease with the increased temperature (Table S1†). Furthermore, the color of the sample gradually changed from black to white (Fig. S4†), *i.e.*, the microstructure begins to change at 350 °C. With the sintering temperature further increasing, the *in situ* oxidation process for MS-600 is thoroughly accomplished. Thus, all of the peaks are ascribed to MoO_3. These results confirm that the MoS_2/MoO_3 heterojunction was successfully obtained.

Scanning electron microscopy (SEM) was utilized to examine the morphology and size of the prepared catalysts. Fig. 2 displays representative morphologies of the synthesized nanocatalysts. MoS_2 (MS-0) exhibits a typical stratified structure (Fig. 2a). However, MoO_3 (MS-600) shows the typical plate-shaped morphology (Fig. 2g). The average size estimate is ~2–5 μm, and is obviously much bigger than the former. As shown in Fig. 2b–f, the formed composites exhibit a gradual change process, corresponding to the characteristics of the monomer MoS_2 and monomer MoO_3. Interestingly, the obtained MoS_2/MoO_3 heterojunction (MS-400) still maintained a lamellar structure that was similar to MoS_2, exhibiting good structural stability. The specific surface area of the MoS_2/MoO_3 heterojunction (MS-400) is 5.9375 m^2 g^{-1}, which is more than twice as much as that for MO-0 (2.7417 m^2 g^{-1}), providing sufficient specific surface areas and active sites for photocatalysis (Fig. S5†). It corresponds with the grain size (Fig. S3†).

The TEM and HRTEM images of the MS-400 nano-composite are displayed in Fig. 3. As shown in Fig. 3a, the MoO_3 layers appear at the outer surface of the MoS_2 crystal. The obvious
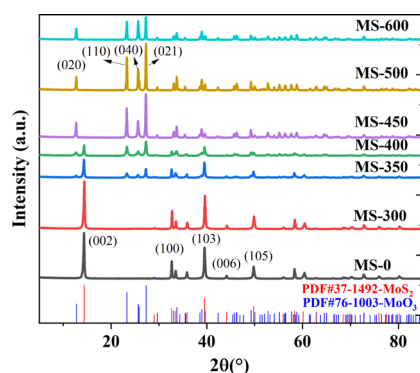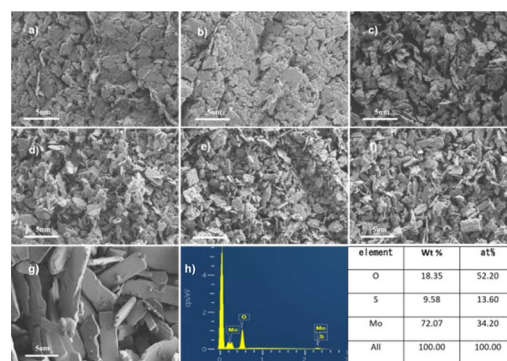

Fig. 1 XRD patterns of the samples.

Fig. 2 SEM images of the samples. (a–g) SEM images of MS-0, MS-300, MS-350, MS-400, MS-450, MS-500 and MS-600. (h) The EDS of MS-400.
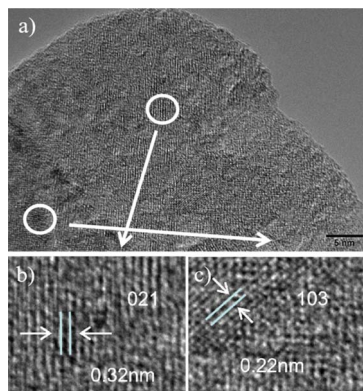
Fig. 3 (a) TEM of the MS-400 nanocatalyst, and HRTEM of (b) MoO_3 and (c) MoS_2.

boundary indicates the presence of a heterostructure and formation *via* the *in situ* oxidation process. In HRTEM, the observed lattice spacing of 0.32 nm clearly corresponds to the (021) planes of MoO_3 (JPCDS 76-1003, Fig. 3b), and the lattice spacing of 0.22 nm corresponds to the (103) plane of MoS_2 (JPCDS 37-1492, Fig. 3c). These results confirm that MoO_3 has been successfully combined with MoS_2, forming a heterojunction between MoS_2 and MoO_3 through *in situ* oxidation.

The chemical state of the samples was carried out using X-ray photoelectron spectroscopy (XPS) measurement. The typical XPS of MS-0, MS-400 and MS-600 are illustrated in Fig. 4. All peaks were calibrated by the C 1s peak at 284.6 eV. Elements of Mo, S, O and adventitious C existed in the MS-0, MS-400 and MS-600 composites (Fig. 4f). High-resolution spectra of Mo 3d (MS-0) are shown in Fig. 4a. Two bands at 229.7 and 232.9 eV are ascribed to the Mo^{4+} $3d_{5/2}$ and $3d_{3/2}$ binding energies, respectively.[43] The Mo $3d_{5/2}$ and Mo $3d_{3/2}$ binding energies for MS-600 are observed at 232.8 and 235.9 eV, respectively, and ascribed to Mo^{6+} (Fig. 4c).[44] Thus, the Mo^{4+}/Mo^{6+} mixed state can be observed in Fig. 4b, and confirms that the MoS_2/MoO_3 heterojunction was successfully obtained. The XPS spectra of S 2p and O 1s for MS-0, MS-400 and MS-600 were also obtained. As shown in Fig. 4d, the decreased S 2p manifests the continuously *in situ*

oxidation process, *i.e.*, MoS_2 gradually converts into MoO_3. It can also be supported by Fig. 4e; *i.e.*, the major peak of O 1s obviously increases with the decreased S 2p. However, O 1s can also be observed in MS-0, which is ascribed to the hydroxyl group from the surface absorbed water, and exhibits an obvious shift that is different from that in MoO_3. All these observations manifest the fabrication of the MoS_2/MoO_3 heterojunction *via* *in situ* oxidation process.

3.2 Photocatalytic performance

The photocatalytic activity of the samples for the degradation of Rhodamine B under LED light is shown in Fig. 5. As shown in Fig. 5a, with increasing sintering temperature, the photocatalytic degradation performance of the samples clearly increases (MS-0-400), and then decreases (MS-450-600). Herein, MS-0 (MoS_2) and MS-600 (MoO_3) exhibit lower intrinsic photocatalytic activities, while MS-400 exhibits the best activity, *i.e.*, the degradation reaches ~56% after 2.5 h under LED light. This indicates that the formation of a heterojunction would be the core issue for photocatalysis. The first order kinetic plots of the samples were performed and are shown in Fig. 5b. The obtained results show that the RhB degradation of the formed heterojunction (MS-400) exhibited 8.0-fold (MS-0)/25.6-fold (MS-600) enhancement when compared to the monomer.

3.3 Optical properties of photocatalyst

Ultraviolet-visible diffuse reflectance spectra (UV-Vis DRS) were used to evaluate the optical properties of the as-prepared samples (Fig. 6a). The sample labeled MS-600 exhibits an absorption edge at around ~450 nm, corresponding to a band gap (E_g) of ~2.75 eV for MoO_3.[45] For MS-0, the absorption edge around ~700 nm manifests a band gap of ~1.77 eV for MoS_2. Due to the unique surface state caused by mixed MoS_2 and MoO_3, MS-400 shows stronger light absorption than MS-0, which is also the reason for the enhanced photocatalytic performance. However, the slight increase in the light absorption causes a remarkable photocatalytic enhancement, indicating the important role of the formed type II heterojunction.

The photoluminescence (PL) spectra of MS-0, MS-400 and MS-600 are displayed in Fig. 6b. The as-prepared samples exhibit a series of peaks at around ~450–480 nm, which is from the recombination of the photo-generated electron and hole pairs.[46] Significantly, compared with MS-0 and MS-600, the PL emission intensity of MS-400 displayed a significant decrease.
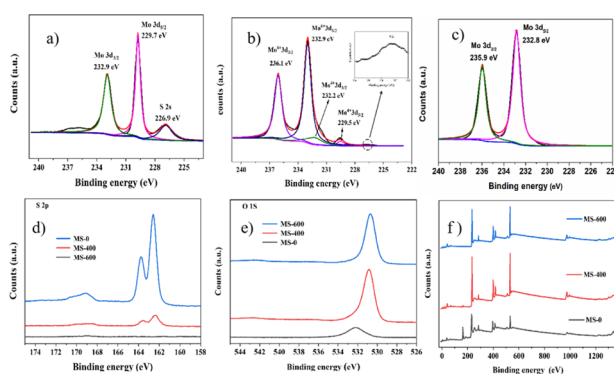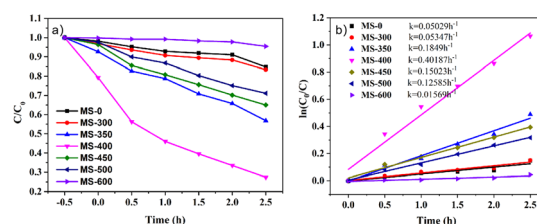

Fig. 4 The Mo 3d and S 2p XPS survey spectra of samples: Mo 3d of (a) MS-0, (b) MS-400, (c) MS-600. (d) The S 2p XPS survey spectra, (e) the O 1s XPS survey spectra, and (f) the XPS full survey spectra.

Fig. 5 (a) Photodegradation efficiency of RhB and (b) the photocatalytic kinetic curves of the RhB degradation.

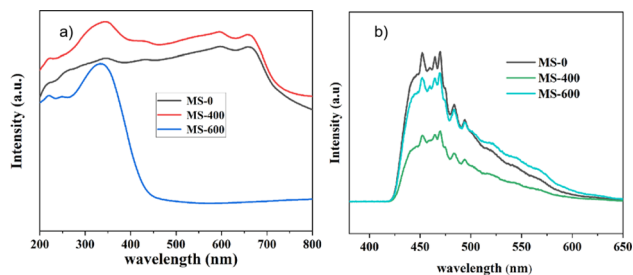© 2024 The Author(s). Published by the Royal Society of Chemistry

Fig. 6 (a) UV-Vis spectra of photocatalysts; (b) Photoluminescence spectra.

This suggests that the recombination rate of the photo-generated electron–hole pairs has been effectively suppressed through the formation of a type II heterojunction structure between MoS_2 and MoO_3. The efficient separation of the photo-generated electron hole pairs leads to enhanced photocatalytic degradation performance, which is consistent with the observed photocatalytic activity of the MS-400 sample.

3.4 Photo-electrochemical measurements of samples

The transient photocurrent responses of MS-0, MS-400 and MS-600 were recorded *via* several on–off cycles of irradiation, as evidence of the activity. MS-400 clearly shows the best photo-current under light irradiation, in comparison with MS-0 (MoS_2) and MS-600 (MoO_3).

The behavior of the photocurrent matches well with the on and off switching of the illumination (Fig. 7a). Electrochemical impedance spectroscopy (EIS) is regarded as an effective approach for investigating the charge transfer process at the interfacial contact,[47] *i.e.*, the arc radius of the EIS Nyquist plot reflects the reaction rate occurring at the interface. As shown in Fig. 7b, the arc radius of MS-400 is smaller than that of MS-0 and MS-600 under light irradiation, indicating that MS-400 exhibited a faster interfacial charge transfer and the most efficient separation of the photogenerated charge carriers. Both results indicate the remarkable optimization of the carrier behaviors, which are beneficial for enhancing photocatalysis.

3.5 Possible photocatalytic mechanism

According to the above discussion, a proposed mechanism is discussed to explain the enhanced photocatalytic activity and stability 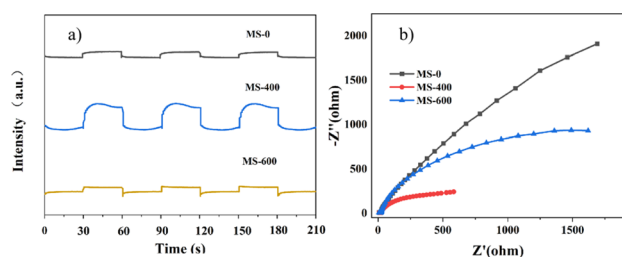of the MoS_2/MoO_3 type II heterostructure under led light irradiation. In this work, the MoO_3 molecule covered the surface of MoS_2 to form the heterojunction. Subsequently, owing to the existence and effect of the built-in electrical potential in the heterostructure, a large amount of electron hole (e^-–h^+) pairs are generated under led light irradiation after the absorption of photons *via* the well-connected interface. Thus, the rapid and effective separation of the electron–hole pairs was accomplished. The electrons accumulating on the surface of MoO_3 will directly reduce the dye molecules, or react with O_2 at the surface of the photocatalyst in the solution to form $\cdot O_2^-$, which could also oxidize the dyes. Furthermore, the holes react directly with the dye or with the water on the catalyst surface to form $\cdot OH$, and then participate in the oxidative degradation of the dye.

Based on the above discussion, the formed MoS_2/MoO_3 heterojunction exhibits decent photocatalytic activities in RhB degradation, owing to the increased specific surface areas/active sites and increased light absorption, including the carrier transportation and separation.

4. Conclusions

In conclusion, a novel MoS_2/MoO_3 type II heterojunction nano-catalyst was successfully synthesized *via* a simple *in situ* oxidation sintering method. The MoS_2/MoO_3 heterojunction exhibits significantly enhanced photocatalytic activity compared to monomer MoS_2 (MS-0, ~8.7-folds) and monomer MoO_3 (MS-600, ~31.5-folds). The improvement of the photocatalytic activity can be mainly ascribed to the existence of a built-in electric field from the MoS_2/MoO_3 type II heterojunction, which can regulate the carrier behavior efficiently to promote the photocatalysis, including the transportation and separation of photogenerated electron and hole pairs, as well as increasing the solar absorption and specific surface areas/active sites *via* microstructure. Thus, this nano-photocatalyst prepared *via in situ* oxidation can provide new insights for the energy-environment field.

Data availability

The data supporting this article have been included as part of the ESI.†

Conflicts of interest

There are no conflicts to declare.

Acknowledgements

Notes and references

1 G. Lin and X. Xu, *ACS Sustain. Chem. Eng.*, 2020, **8**, 9641–9649.

Fig. 7 (a) *i*–*t* curves of the samples. (b) Electrochemical impedance spectra (EIS) of the samples.

2 H. Liu, J. Wang, O. Odunmbaku, P. Xia, L. Liu, Q. Chang, Y. Huang, X. lin, J. Yang, Z. Shang, Z. Ye, M. Li and J. Qiu, *Sep. Purif. Technol.*, 2023, **320**, 124142.

3 X. Ren, M. Guo, L. Xue, L. Xu, L. Li, L. Yang, M. Wang, Y. Xin, F. Ding and Y. Wang, *Appl. Surf. Sci.*, 2023, **630**, 157446.

4 C. Zhang, L. Wang, F. Yuan, R. Meng, J. Chen, W. Hou and H. Zhu, *Appl. Surf. Sci.*, 2020, **534**, 147544.

5 A. Singh, S. S. Shah, C. Sharma, V. Gupta, A. K. Sundramoorthy, P. Kumar and S. Arya, *J. Environ. Chem. Eng.*, 2024, **12**, 113032.

6 V. Vaiano, G. Iervolino, D. Sannino, L. Rizzo, G. Sarno and A. Farina, *Appl. Catal., B*, 2014, **160**, 247–253.

7 H. Wang, X. Huang, W. Li, J. Gao, H. Xue, R. K. Y. Li and Y.-W. Mai, *Colloids Surf., A*, 2018, **549**, 205–211.

8 W. G. Wang, J. G. Yu, Q. J. Xiang and B. Cheng, *Appl. Catal., B*, 2012, **119**, 109–116.

9 Y. F. Zhang, S. S. He, Z. L. He, Y. C. Zhang, Y. P. Feng, Y. L. Wang and M. Zhang, *Int. J. Electrochem. Sci.*, 2022, **17**, 13.

10 M. Thakur, A. Singh, A. Dubey, A. K. Sundramoorthy, P. Kumar and S. Arya, *Emerg. Mater.*, 2024, **7**, 1805–1817.

11 K. Chawraba, H. Medlej, A. Noun, M. Sakr, J. Toufaily, J. Lalevee and T. Hamieh, *Chemistryselect*, 2024, **9**, 13.

12 B. Singh, A. Singh, A. Sharma, P. Mahajan, S. Verma, B. Padha, A. Ahmed and S. Arya, *J. Mol. Struct.*, 2022, **1255**, 132379.

13 A. Singh, A. Ahmed, A. Sharma, C. Sharma, S. Paul, A. Khosla, V. Gupta and S. Arya, *Phys. B*, 2021, **616**, 413121.

14 A. Dubey, A. Singh, A. Sharma, A. K. Sundramoorthy, R. Mahadeva, V. Gupta, S. Dixit and S. Arya, *Appl. Phys. A*, 2023, **129**, 692.

15 M. Bhagat, R. Anand, R. Datt, V. Gupta and S. Arya, *J. Inorg. Organomet. Polym. Mater.*, 2019, **29**, 1039–1047.

16 M. T. L. Lai, K. M. Lee, T. C. K. Yang, C. W. Lai, C.-Y. Chen, M. R. Johan and J. C. Juan, *J. Alloys Compd.*, 2023, **953**, 169834.

17 A. Xiakeer, L. Wang, M. Maimaiti, M. Jiang, X. Feng and Y. Zhang, *Ceram. Int.*, 2024, **50**, 2680–2688.

18 Y. H. Fu, W. Liang, J. Q. Guo, H. Tang and S. S. Liu, *Appl. Surf. Sci.*, 2018, **430**, 234–242.

19 J. W. Fu, Q. L. Xu, J. X. Low, C. J. Jiang and J. G. Yu, *Appl. Catal., B*, 2019, **243**, 556–565.

20 Z. Tang, L. Xu, K. Shu, J. Yang and H. Tang, *Colloids Surf., A*, 2022, **642**, 128686.

21 Y. Yuan, R.-t. Guo, L.-f. Hong, X.-y. Ji, Z.-s. Li, Z.-d. Lin and W.-g. Pan, *Colloids Surf., A*, 2021, **611**, 125836.

22 S. Dutt, A. Singh, R. Mahadeva, A. K. Sundramoorthy, V. Gupta and S. Arya, *Diamond Relat. Mater.*, 2024, **141**, 110554.

23 R. Yang, Y. Fan, Y. Zhang, L. Mei, R. Zhu, J. Qin, J. Hu, Z. Chen, Y. Hau Ng, D. Voiry, S. Li, Q. Lu, Q. Wang, J. C. Yu and Z. Zeng, *Angew. Chem., Int. Ed.*, 2023, **62**, 13.

24 L. Britnell, R. M. Ribeiro, A. Eckmann, R. Jalil, B. D. Belle, A. Mishchenko, Y.-J. Kim, R. V. Gorbachev, T. Georgiou, S. V. Morozov, A. N. Grigorenko, A. K. Geim, C. Casiraghi, A. H. Castro Neto and K. S. Novoselov, *Science*, 2013, **340**, 1311–1314.

25 F. Jamal, A. Rafique, S. Moeen, J. Haider, W. Nabgan, A. Haider, M. Imran, G. Nazir, M. Alhassan, M. Ikram, Q. Khan, G. Ali, M. Khan, W. Ahmad and M. Maqbool, *ACS Appl. Nano Mater.*, 2023, **6**, 7077–7106.

26 W. K. Jo and N. C. S. Selvam, *Appl. Catal., A*, 2016, **525**, 9–22.

27 N. N. Meng, Y. F. Zhou, W. Y. Nie, L. Y. Song and P. P. Chen, *J. Nanopart. Res.*, 2015, **17**, 10.

28 L. Yang, S. H. Guo and X. H. Li, *J. Alloys Compd.*, 2017, **706**, 82–88.

29 A. Nazneen, M. I. Khan, M. A. Naeem, M. Atif, M. Iqbal, N. Yaqub and W. A. Farooq, *J. Mol. Struct.*, 2020, **1220**, 6.

30 Y. Yuan, P. F. Shen, Q. J. Li, G. Chen, H. F. Zhang, L. Y. Zhu, B. Zou and B. B. Liu, *J. Alloys Compd.*, 2017, **700**, 12–17.

31 D. Voiry, J. Yang and M. Chhowalla, *Adv. Mater.*, 2016, **28**, 6197–6206.

32 S. Balendhran, S. Walia, H. Nili, J. Z. Ou, S. Zhuiykov, R. B. Kaner, S. Sriram, M. Bhaskaran and K. Kalantar-zadeh, *Adv. Funct. Mater.*, 2013, **23**, 3952–3970.

33 Z. Wei and S. Zhuiykov, *Nanoscale*, 2019, **11**, 15709–15738.

34 J. Liu, S. Shao, G. Fang, J. Wang, B. Meng, Z. Xie and L. Wang, *Sol. Energy Mater. Sol. Cells*, 2014, **120**, 744–750.

35 T. Brezesinski, J. Wang, S. H. Tolbert and B. Dunn, *Nat. Mater.*, 2010, **9**, 146–151.

36 X. Xue, J. Zhang, I. A. Saana, J. Sun, Q. Xu and S. Mu, *Nanoscale*, 2018, **10**, 16531–16538.

37 J. F. Qiu, J. Q. Pan, S. H. Wei, Q. F. Liang, Y. W. Wang, R. Wu and C. R. Li, *RSC Adv.*, 2021, **11**, 38523–38527.

38 Z. L. Huang, J. C. Liu, S. Zong, X. Y. Wang, K. X. Chen, L. L. Liu and Y. X. Fang, *J. Colloid Interface Sci.*, 2022, **606**, 848–859.

39 M. K. Hussain and N. R. Khalid, *J. Mol. Liq.*, 2022, **346**, 11.

40 M. K. Hussain, N. R. Khalid, M. B. Tahir, M. Tanveer, T. Iqbal and M. Liaqat, *Mater. Sci. Semicond. Process.*, 2023, **155**, 11.

41 T. Liu, J. Huang, Z. Huang, Q. Luo, H. Wu, Y. Meng, C. He and H. Li, *Chem. Eng. J.*, 2024, **486**, 150209.

42 Z. Huang, J. Huang, T. Liu, Y. Wen, H. Wu, S. Yang and H. Li, *Chem. Eng. J.*, 2024, **485**, 149987.

43 S. W. Hu, L. W. Yang, Y. Tian, X. L. Wei, J. W. Ding, J. X. Zhong and P. K. Chu, *Appl. Catal., B*, 2015, **163**, 611–622.

44 H. D. Li, W. J. Li, X. T. Liu, C. J. Ren, F. Z. Wang and X. Miao, *J. Taiwan Inst. Chem. Eng.*, 2018, **89**, 86–94.

45 J. Ma, Q. Liu, L. Zhu, J. Zou, K. Wang, M. Yang and S. Komarneni, *Appl. Catal., B*, 2016, **182**, 26–32.

46 W. Zhang, S.-c. Li, M. Yan, L. Li, J. Ma, J. Wang, C. Liu and Y. Bao, *J. Environ. Chem. Eng.*, 2022, **10**, 108418.

47 W. Teng, X. Li, Q. Zhao and G. Chen, *J. Mater. Chem. A*, 2013, **1**, 9060–9068.